THE JOURNAL OF PHYSICAL CHEMISTRY C

C: Physical Processes in Nanomaterials and Nanostructures

Dipolar Magnetic Interactions in Mn-Doped Magnetite Nanoparticles Loaded into PLGA Nanocapsules for Nanomedicine Applications

Lucia Del Bianco, Federico Spizzo, Paolo Sgarbossa, Elisabetta Sieni, Gianni Barucca, Maria Rosaria Ruggiero, and Simonetta Geninatti Crich

J. Phys. Chem. C, **Just Accepted Manuscript** • DOI: 10.1021/acs.jpcc.9b09146 • Publication Date (Web): 16 Nov 2019

Dipolar Magnetic Interactions in Mn-doped Magnetite Nanoparticles Loaded into PLGA Nanocapsules for Nanomedicine Applications

L. Del Bianco[1]*, F. Spizzo[1], P. Sgarbossa[2], E. Sieni[3], G. Barucca[4], M. R. Ruggiero[5], S. Geninatti Crich[5]

[1] Dipartimento di Fisica e Scienze della Terra, Università di Ferrara, I-44122 Ferrara, Italy

[2] Dipartimento di Ingegneria Industriale, Università di Padova, I-35131 Padova, Italy

[3] Dipartimento di Scienze Teoriche e Applicate – DiSTA, Università dell'Insubria, I-21100 Varese, Italy

[4] Dipartimento SIMAU, Università Politecnica delle Marche, I-60131 Ancona, Italy

[5] Dipartimento di Biotecnologie Molecolari e Scienze per la Salute, Università di Torino, I-10126 Torino, Italy

*Corresponding author. E-mail address: lucia.delbianco@unife.it

Abstract

Nanocapsules made of PLGA copolymer and with a different load of oleate-coated Mn-doped magnetite nanoparticles are studied for potential nanomedicine applications as nanocarriers with magnetic functionalities, in particular magnetic heating. The mean size of the PLGA nanocapsules and of the magnetic nanoparticles is around 200 nm and 8 nm, respectively. The aim is to study to what extent the different concentration of magnetic nanoparticles and their confinement into the PLGA nanocapsules affect their spatial arrangement and their magnetic interaction. This is crucial for making progress in the field of magnetic nanocarriers, tailoring their magnetic properties and thus optimizing their performance.

The results obtained by combining structural and magnetic analyses indicate that the nanoparticles form aggregates into the PLGA nanocapsules - reaching larger dimension in the sample with the higher magnetic load - and that the dipolar interactions rule the magnetization process and the magnetic relaxing behaviour, which are factors determining the magnetic heating capacity. In particular, a double role of the dipolar interactions in the magnetic heating mechanism is highlighted: they stabilize the magnetic moments of the nanoparticles against superparamagnetism and give rise to low-remanence magnetic configurations of the nanoparticle aggregates. While the first effect enhances the heating efficiency, the second one appears harmful.

1. INTRODUCTION

During the last decade the studies on the applications of magnetic nanoparticles in nanomedicine have been impelled by the growing interest for theranostics, namely the creation of medical platforms able to combine therapeutic and diagnostic functions.[1,2,3,4] In fact, magnetic nanoparticles can be considered as intrinsic theranostic elements since they can act simultaneously as magnetic contrast enhancers in magnetic resonance imaging (MRI) and as hyperthermia agents, under an alternating magnetic field, in the treatment of cancer.[5,6,7] Moreover, magnetic nanoparticles coated with biocompatible surfactants (polymers, such as dextran or PEG, as well as inorganic materials, such as silica or gold) and functionalized to bind drug molecules and/or biotargeting agents (antibodies, proteins, hormones, etc.) can be used for targeted drug delivery driven by a magnetic field gradient.[8, 9, 10, 11, 12]

Indeed, the functionalities of magnetic nanoparticles can be expanded, combined and tuned by using them in the formulation of hybrid nanocomposite materials. An extraordinary variety of magnetic systems has been created, consisting of nanoparticles - often made of spinel iron oxides due to their good biocompatibility, compared to other magnetic phases – embedded in a matrix, whose chemical and structural characteristics determine the possible use of the final material. Thus, magnetic nanoparticles have been incorporated in different types of polymeric matrices, [13, 14, 15, 16, 17] dendrimers,[18] hydrogels,[19, 20, 21] liquid crystals[22] as well as in cellulose,[23] silk[24] and biomimetic hydroxyapatite,[25] for applications ranging from drug delivery and release,[26, 27] to production of biomimetic magnetic scaffolds for tissue regeneration,[28, 29] to magnetic field driven actuators.[30, 31]

In other formulations, the magnetic nanoparticles are loaded on nanocarriers, namely the matrix in which they are encapsulated is also structured on the nanometric scale. Also in this case, materials of different nature have been employed, such as polymers,[32, 33] mesoporous silica nanoparticles,[34] liposomes.[35, 36, 37] In this field, some studies have been reported about magnetic nanoparticles in nanocapsules of poly(lactic-co-glycolic acid) (PLGA),[38, 39, 40, 41, 42] a copolymer approved for human use, largely used for drug delivery applications due to its good biodegradability and biocompatibility.[43, 44]

The incorporation of magnetic nanoparticles, with size of the order of 10 nm, in PLGA nanocapsules, with typical size of the order of 100 nm, is aimed at realizing highly biocompatible vectors, which, by virtue of their magnetic functionality, can be possibly driven to a specific target, where they can release their load. Together with the nanoparticles themselves, the load may consist

of drug molecules, bound to the nanoparticles or encapsulated separately in the PLGA. One of the main advantages of this formulation is that the release can be favored and controlled by exploiting the magnetic heating to thermally promote the PLGA nanocapsule destruction.

It is to be noted that in most preparations the nanoparticles are stabilized toward aggregation by coating with oleate, which is insoluble in water.[45, 46, 47] Hence, another important advantage of incorporating the nanoparticles in PLGA is to allow their dispersion in water and thus increase their bioavailability.

From the magnetic point of view, the nanocarriers constitute very interesting systems in which the magnetic nanoparticles are spatially confined at the nanoscale and generally subjected to interparticle dipolar magnetic interactions. The nanoparticles are not free to move and their spatial arrangement depends to some extent on the geometric and structural features of the nanocarriers into which they are loaded. The arrangement of the nanoparticles may affect the way in which they interact magnetically and vice versa. In turn, the magnetic interactions influence the magnetic configuration of the magnetic moments of the nanoparticles [48, 49] and alter the magnetic relaxation processes,[50] which are factors closely related to the heating efficiency.[47, 51, 52, 53, 54, 55]

The magnetic properties of the nanocarriers also depend on the concentration of the loaded nanoparticles, which is established on the basis of the specific envisaged application. As general attention, the magnetic load should not be so high as to excessively increase the mass density of the nanocarriers since this can reduce their dispersion stability and lead to sedimentation effects. A high fraction of magnetic nanoparticles is advisable, for instance, to enable external magnetic guidance of the magnetic nanocarriers,[38] whereas a lower fraction may be sufficient for promoting the degradation of the PLGA by magnetic heating.[40] However, changing the concentration of magnetic nanoparticles can clearly influence the strength of the interparticle magnetic interactions and hence modify the functionality of the nanocarriers in an unexpected or unwanted way.

In this work, this specific item is addressed through the experimental study of PLGA nanocapsules loaded with oleate-coated Mn-doped magnetite nanoparticles. The Mn-doping, namely the substitution of Fe^{2+} ions with Mn^{2+} ions in the spinel structure of Fe_3O_4, is expected to enhance the saturation magnetization of magnetite,[52, 56, 57, 58] thus compensating, at least in part, for the detrimental effect of the spin-canting phenomenon, which usually decreases the magnetization of magnetic nanoparticles compared to the bulk counterpart.[59, 60, 61] The improvement of the saturation magnetization is beneficial both for the magnetic heating efficiency and for the magnetic

transport.[62, 63] Moreover, it has been reported that the Mn-doping can increase the contrast ability of magnetite nanoparticles in MRI.[58, 64]

Therefore, our study concerns potentially interesting samples for nanomedicine applications and the main objective is to clarify the complex relationship between the structural properties of the nanoparticles, their spatial configuration, as determined by the circumstance of being entrapped into the PLGA nanocapsules, and their magnetic behavior.

We report about two selected samples with a markedly different load of magnetic nanoparticles. In both cases, the weight fraction of the magnetic nanoparticles is in minority with respect to the whole sample mass, which is in favor of a possible use for controlled drug release in combination with magnetic heating.

The purpose of our study is pursued by investigating the magnetic properties of the PLGA nanocapsules and their dependence on the amount of loaded nanoparticles by SQUID magnetometry and ^{1}H Nuclear Magnetic Relaxation Dispersion (NMRD) profiles, in combination with compositional and structural analyses by different techniques, in particular electron microscopy (TEM, SEM). The obtained results are correlated to the magnetic heating capacity of the samples, highlighting the decisive role of the dipolar magnetic interactions. This methodological approach is crucial in order to make progress in the field of magnetic nanocarriers in the direction of being able to tailor their functions and optimize their performance.

2. MATERIALS AND METHODS

2.1 Preparation of the samples

2.1.1 Synthesis of the Mn-doped magnetite nanoparticles

The oleate-coated Mn-doped magnetite nanoparticles are produced by thermal decomposition from organometallic precursors, following the method developed by S. Sun et al.,[45] as we have described elsewhere.[52] Typically, 2.12 g (6.00 mmol) of iron(III) acetylacetonate, [Fe(acac)$_3$], and 0.76 g (3.00 mmol) of manganese(II) acetylacetonate, [Mn(acac)$_2$], are mixed with 5.65 g (20.0 mmol) of oleic acid, 5.35 g (20.0 mmol) of oleylamine, and 6.91 g (30.0 mmol) 1,2-tetradecanediol in 100 ml of benzyl ether, under nitrogen atmosphere. The dark red solution is magnetically stirred and heated with a mantle at 200°C for 120 minutes and then at 300°C for 150 minutes. After cooling the black suspension to room temperature, it is poured in 300 ml of ethanol and magnetically separated. The obtained nanoparticles are washed three times with 50 ml of ethanol and dried under vacuum. For

the preparation of the magnetic PLGA samples, the nanoparticles are redispersed in n-octane and stored as 10 mg/mL suspension.

The Mn-doped magnetite nanoparticles obtained through this procedure are labelled as MagNPs.

In the 10 mg/mL of MagNPs suspension the amount of Fe and Mn, as assessed by the ICP-MS elemental analysis, are (84 ± 2) mM and (16.5 ± 0.5) mM, respectively, corresponding to a Mn/Fe atomic ratio of (0.20 ± 0.01).

2.1.2 Synthesis of the samples of PLGA + MagNPs

The samples of PLGA + MagNPs are obtained using an oil-in-water (o/w) emulsion solvent extraction method. The emulsion is prepared by dissolving 25 mg of Poly(D,L-lactide-co-glicolide) (PLGA) (RG 502H 50:50, average molecular weight (Mw) 30 000–60 000 Da) and MagNPs in 0.5 mL of chloroform, called phase 1. Two samples are prepared with two different amounts of MagNPs belonging to the very same batch: 10 mg and 1 mg per 25 mg of PLGA, respectively. The sample prepared with higher concentration of magnetic nanoparticles is labelled PHC, whereas the one with lower concentration is labelled PLC.

Phase 2 consists of 3% w/v poly (vinyl alcohol) (PVA), Mw 31 000–50 000 Da (98%–99% hydrolyzed) aqueous solution (3 ml). Phase 1 is added into phase 2 drop by drop and sonicated with a tip sonicator (UW2070, Bandelin electronic, Berlin) for 300 s at 100% power. The final emulsion is transferred to a 100 mL round-bottomed flask and put into a rotary evaporator at 740 mmHg and 30 rpm for 150 min to remove the organic solvent. The excess of PVA is removed washing the emulsion by ultrafiltration using vivaspin filters (Sartorius) (cutoff 1×10^6 Da) by centrifugation at 2655 rcf three times with 20 mL of NaCl (0.15 mM) /Hepes (5mM) buffer (HBS). Centrifugation is applied to force solvent through the membrane, leaving a more concentrated sample in the upper chamber. During ultrafiltration also the magnetic nanoparticles which do not remain entrapped into the PLGA nanocapsules are removed by the solution. At the end of the synthetic process, the two PLGA+MagNPs preparations are suspended in HBS buffer. For the magnetic measurements, 1 mL of PHC and PLC is lyophilized in high vacuum. The entrapment yield is of 44% and 51% for PHC and PLC respectively, obtained by measuring Mn and Fe concentrations in the final solutions by ICP-MS. A preparation of PLGA without magnetic load, indicated as $PLGA_{Ref}$, is used as reference sample.

2.2 Characterization techniques

Transmission electron microscopy (TEM) observations are carried out using a TECNAI FEI G2 microscope. For this purpose, the MagNPs are dispersed in n-hexane whereas the two PLGA+MagNPs preparations are further diluted in water; then a drop of the suspension is cast on a carbon coated copper grid for the analysis.

Scanning electron microscopy (SEM) observations are performed on the PLGA+MagNPs and $PLGA_{Ref}$ samples, in the form of liquid suspensions, by means a Zeiss Supra 40 field-emission microscope (Carl Zeiss Microscopy GmbH, Jena, Germany). To this end, a drop of suspension is deposited on a commercial aluminum stub and kept in air until complete evaporation of the solvent. Due to the low accelerating voltage used in the SEM (5kV), the samples are observed without any conductive coating.

The amount of Fe and Mn in MagNPs, PLC and PHC is assessed by using inductively coupled plasma mass spectrometry (ICP-MS; Element-2; Thermo-Finnigan, Rodano (MI), Italy). Sample digestion is performed by means of microwave heating for 14 min at 160 °C in 1 mL of concentrated HNO_3 (70%) (Milestone, Ethos Up Microwave Digestion System, Bergamo, Italy).

Dynamic light scattering (DLS) measurements are carried out on PHC and PLC using a Malvern Zetasizer 3000HS (Malvern, UK). The PHC and PLC samples are analyzed at temperature T = 25 °C in filtered (cutoff, 200 nm) HBS buffer (pH 7.4). The particle size distribution is derived from a deconvolution of the measured intensity autocorrelation function of the sample using a non-negatively constrained least squares (NNLS) fitting algorithm, a common examples being CONTIN.

The magnetic properties of MagNPs, PHC and PLC are studied on the samples in the dried form by a superconducting quantum interference device (SQUID) magnetometer operating in the 5 – 300 K temperature range (maximum applied field H_{appl} = 50 kOe, sensitivity 10^{-7} emu). The weight of the samples is measured with a precision of 10^{-5} g in order to evaluate the specific magnetization (magnetic moment/sample mass).

$1/T_1$ nuclear magnetic relaxation dispersion (NMRD) profiles of PHC and PLC are measured, at temperature T = 25 °C, over a continuum of magnetic field strength from 0.00024 to 0.24 T

(corresponding to 0.01–10 MHz proton Larmor frequency), on the fast field cycling (Stelar SMARTRACER). The relaxometer operates under complete computer control with an absolute uncertainty in the $1/T_1$ values of ±2%. The typical field sequences used are the non-polarized (NP) sequence between 10 and 7 MHz and pre-polarized (PP) sequence between 7 and 0.01 MHz. The observation field is set at 7.2 MHz while the polarization field at 9 MHz. T_1 is determined by the saturation recovery method. 16 values of delay between pulses are used.

Magnetic heating tests are carried out on the samples in the form of suspension, in an alternating magnetic field in a custom-made apparatus equipped with a 7-turns inductor, 8 cm internal diameter, 15 cm long, supplied by an EASYHEAT L1 5060 10.0 kW (Ambrell) generator.[65] The temperature is measured by a Optocom Fotemp-1H thermometer with a TS3/2 fiber optic.

3. RESULTS AND DISCUSSION

3.1 Structure and composition of the Mn-doped magnetite nanoparticles

The ferrite cubic spinel structure of the produced nanoparticles (sample MagNPs) is confirmed by the X-ray diffraction (XRD) analysis. The spectrum features broad diffraction peaks corresponding to the structure of magnetite (Figure S1, Supporting Information). Indeed, the XRD investigation cannot provide evidence of Mn-doping in the produced magnetic nanoparticles because Fe_3O_4 and $MnFe_2O_4$ are isostructural phases and the values of the interplanar distances are too close for the diffraction peaks to be resolved. The Mn-doping is demonstrated by the value of the Néel temperature (T_N) in MagNPs, measured by thermogravimetric analysis method (TGA) in a magnetic field gradient (Figure S2, Supporting Information). In fact, $T_N \sim 517$ °C, well below the nominal value of bulk Fe_3O_4 (585 °C). This value of T_N is in perfect agreement with that we measured in nanoparticles synthesized following the very same method and that was compared to $T_N \sim 583$ °C of pure magnetite nanoparticles of similar size.[52] Moreover, the TGA analysis does not detect T_N of Fe_3O_4 and $MnFe_2O_4$, which is in favor of a uniform Mn-doping of the magnetic nanoparticles.

The presence of oleate around the nanoparticles is confirmed by the Fourier transform infrared spectroscopy (FT-IR) analysis. In the spectrum for MagNPs (Figure S3, Supporting Information), the bands at 1410 cm^{-1}, 1543 cm^{-1}, 2850-2920 cm^{-1}, and 3370 cm^{-1} are for C-H_{rock} and asymmetric $COO_{stretch}$, C=$C_{stretch}$ and symmetric $COO_{stretch}$, C-$H_{stretch}$ and residual O-$H_{stretch}$, respectively. The

bands at 392 cm^{-1} and 573 cm^{-1} are related to the iron-oxide phase. No other signal is visible. Hence, we exclude the presence of reaction byproducts and of free oleic acid. Regarding the latter, the FT-IR spectrum for oleic acid shows, in particular, two signals at 1707 cm^{-1} and 939 cm^{-1}, which correspond to the $C=O_{stretch}$ and to the out-of-plane $O\text{-}H_{stretch}$, respectively (Figure S3, Supporting Information). These two features are not visible in the spectrum for MagNPs. In fact, they disappear when the oleic acid is deprotonated to the corresponding oleate ion, whose carboxylate group (COO^-) gives only the two asymmetric and symmetric $COO_{stretch}$ which fall respectively in the 1410 and 1543 cm^{-1} bands observed in the MagNPs spectrum. It follows that the oleate ions must be coordinated on the surface of the magnetic nanoparticles.

The weight fraction of oleate in MagNPs is ~ 15%, as estimated by TGA (without magnetic field gradient) measuring the mass loss ascribed to its decomposition (Figure S4, Supporting Information).

A bright field TEM image of the MagNPs sample is shown in Figure 1a. The nanoparticles tend to self-order on the carbon grid, a tendency favored by the quite regular morphology and uniform size as well as by the presence of the oleate coating which prevents the contact between them. The distribution in size (D) of the nanoparticles, obtained from TEM images, is shown in Figure 1b: the mean size $\langle D \rangle = (8.4 \pm 0.4)$ nm and the standard deviation $\sigma = 2.2$ nm (a population of about 300 nanoparticles has been considered).

3.2 Structural properties of the PLGA + MagNPs samples

A typical SEM image of the PLGA+MagNPs samples is shown in Figure 2a. In particular, it refers to PHC, but very similar results are obtained for PLC and also for $PLGA_{Ref,}$ actually. In the picture, objects producing a similar white contrast are visible and they correspond to PLGA nanocapsules of mean size around 200 nm (small size bright spots visible in the background of the SEM image are HBS buffer residues). This is in good agreement with the DLS analysis, which indicates hydrodynamic size values $D_{hyd} = (216 \pm 3)$ nm and $D_{hyd} = (211 \pm 6)$ nm for PHC and PLC respectively, equal within the experimental error (see Figure S5, Supporting Information).

TEM images of PHC and PLC samples are shown in Figure 2b-c and Figure 2d-e, respectively. The magnetic nanoparticles appear as dark elements on a quite uniform light-gray background since the PLGA does not produce enough contrast for the nanocapsules to be distinguished. The microscopy analysis confirms that the concentration of magnetic nanoparticles is definitely higher in PHC than in PLC. Indeed, in carrying out the TEM observations on PLC, it is even difficult to come across

the magnetic nanoparticles. We observe that the nanoparticles tend to arrange in form of aggregates, as a result of being confined into the PLGA nanocapsules. However, larger aggregates, i.e. formed by a greater number of nanoparticles, exist in PHC compared to those visible in PLC. In this last sample, clusters of just a few nanoparticles can be observed mostly. The aggregates of nanoparticles in PHC - which in some cases are as large as 100 nm or even more - tend to assume a spherical shape and, as their size increases, they show a more and more rounded profile.

In none of the two samples the magnetic nanoparticles appear homogeneously distributed in space. Considering the distribution in size of the aggregates visible in the images, one can infer that, most likely, some PLGA nanocapsules are well filled with magnetic nanoparticles, whereas a poor magnetic load or no load at all exists in others. This finding is in line with what reported by Liu et al. for similar samples.[38] In particular, the authors explain that, thanks to the oleate coating, the magnetite nanoparticles are hydrophobic and, in this condition, they prefer the oil phase over the aqueous phase. Hence, a relatively smaller amount of nanoparticles is lost during the emulsion formation, compared to the case in which they are naked and hydrophilic. However, the authors also warn that a heterogeneous distribution of magnetic nanoparticles in the PLGA should be expected unless the miscibility between the oleic acid and the polymer is very high.

3.3 Magnetic properties

3.3.1 Magnetization measurements

Magnetic hysteresis loops are measured on MagNPs, PHC and PLC, in the dried form, at different temperatures T in the 5-300 K range. The loops at T = 5 K are shown in Figure 3a-c. The specific magnetization M is reported, obtained by normalizing the magnetic moment to the mass of the sample. Regarding MagNPs, the mass is that of the magnetic nanoparticles plus the fraction of oleate (~15 wt. %, as estimated by TGA). For PHC and PLC, the mass weighted after lyophilization includes, besides PLGA and MagNPs (i.e. the magnetic nanoparticles with oleate), residual PVA, buffer salts and residual water molecules.

At T = 5 K, the magnetization of MagNPs measured at the field H=50 kOe, that we indicate as M_{50kOe}, is (73.7 ± 0.7) emu/g (Figure 3a). The value of M_{50kOe} that one can calculate excluding the mass of oleate is obviously higher and equal to (86.7 ± 1.7) emu/g. As we already reported,[52] thanks to the Mn doping, quite high values of magnetization are obtained both at T = 5 K and at T = 300 K (Table 1), in spite of the small nanoparticle size, lower than 10 nm, which enhances the spin canting effect. M_{50kOe} measured in PHC is higher than that in PLC, in line with the different concentration of magnetic nanoparticles in the two samples (Figure 3b-c). A non-saturating tendency is

particularly well visible in the loop of PLC, consistent with the existence of a paramagnetic signal superposed to the ferromagnetic one.

The thermal dependence of M_{50kOe} is measured between 5 and 300 K. In Figure 3d, the curves of M_{50kOe} vs. T are shown as normalized to their final values at T = 300 K. The existence of a paramagnetic contribution in PHC and PLC is confirmed by the divergence of the magnetization for T tending to zero. Since this behavior is also visible in the M_{50kOe} vs. T curve of sample $PLGA_{Ref}$ (Figure S6, Supporting Information), it is evident that the paramagnetic contribution comes from the PLGA and is particularly remarkable in PLC because of the smaller ferromagnetic signal provided by the magnetic nanoparticles.

M_{50kOe} measured at T = 5 K and 300 K on PHC and PLC are reported in Table 1. Comparing the value of M_{50kOe} at T = 300 K with that measured at the same temperature on MagNPs [(58.2 ± 0.6) emu/g], we can estimate the weight fraction of loaded magnetic nanoparticles (the room temperature values are considered in order to minimize the influence of the paramagnetic contribution of PLGA). The results are shown in Table 1: the nanoparticle concentration is ~ 5.3 wt. % and ~ 0.72 wt. % for PHC and PLC, respectively.

Having estimated the amount of magnetic nanoparticles in PHC and PLC and considering the value of M_{50kOe} of MagNPs at T = 5 K, we can calculate the contribution of the magnetic nanoparticles only to the magnetization at that temperature. We indicate this parameter as M^*_{50kOe}. We obtain M^*_{50kOe} ~3.9 emu/g for PHC and M^*_{50kOe} ~ 0.53 emu/g for PLC. Now, we derive the squareness at T = 5 K, defined as M_r/ M^*_{50kOe}, where M_r is the remanent magnetization in the hysteresis loops of Figure 3a-c. The squareness is ~ 0.30 and ~ 0.37 in PHC and PLC respectively and ~ 0.15 in MagNPs (obviously M_{50kOe} and M^*_{50kOe} coincide for MagNPs) (Table 1). The values of the coercivity H_C at T = 5 K are also reported in Table 1 (we have verified that manually subtracting the paramagnetic signal of PLGA from the loops in Figure 3b-c does not alter their shape at all, for $|H| \leq 5$ kOe). They are quite close to each other, between ~ 177 Oe and ~190 Oe. H_C decreases rapidly on increasing T (Figure 3e) and at T = 300 K, no magnetic hysteresis is observed in the three samples (i.e. H_C and M_r are null), which is consistent with a superparamagnetic behavior of the magnetic nanoparticles, in the adopted experimental conditions.

3.3.2 Magnetic interactions

To gain information on the nature and strength of magnetic interactions in the samples, the isothermal remanent magnetization (IRM) and the dc demagnetization remanence (DCD) are

measured at T = 5 K, following a standard a procedure.[25, 66] IRM is measured on an initially demagnetized sample that is progressively magnetized by a positive magnetic field increasing from 0 Oe up to 35 kOe; DCD is measured on a sample initially brought to saturation by a negative magnetic field and then progressively magnetized by a positive field increasing from 0 Oe up to 35 kOe. The recorded remanence values are plotted as a function of the previously applied magnetic field. The IRM curve is normalized to the final recorded value of remanence and indicated as Ir; the DCD curve is normalized to the initial value and indicated as Id. The Ir and Id curves measured on MagNPs, PHC and PLC are shown in Figure 4a-b.

As derived by Wohlfarth,[67] for an assembly of non-interacting single-domain particles, the two remanence curves are connected by the relation:

$$Id(H) = 1-2Ir(H) \qquad (1)$$

It follows that the plot of Id(H) vs. Ir(H), i.e. the Henkel plot,[68] exhibits a linear trend. Deviations from linearity reveal the presence of interparticle magnetic interactions.[69] The Henkel plots for the three samples are shown in Figure 4c: they exhibit an upward concavity, characteristic of systems ruled by demagnetizing magnetic interactions of dipolar nature.

From the remanence curves in Figure 4a-b, one can derive the isothermal remanence coercivity H_{C_Ir}, which corresponds to the field at which Ir = 0.5, and the demagnetization remanence coercivity H_{C_Id}, which is the field at which Id vanishes.[69] The two parameters are respectively a measure of the difficulty of magnetizing and of demagnetizing the system and, while the coercivity H_C is determined by reversible and irreversible magnetization processes, they are related to irreversible changes only. The values of H_{C_Ir} and H_{C_Id} at T = 5 K are reported in Table 2. In the case of non-interacting nanoparticles, equation (1) states that H_{C_Ir} and H_{C_Id} should be equal. On the contrary, we found that $H_{C\_Ir} > H_{C\_Id}$, as expected for systems more difficult to magnetize than to demagnetize, namely that are governed by predominant dipolar interactions, in line with the Henkel plots trend. Accordingly, we define an effective interaction field $IF = (H_{C\_Ir} - H_{C\_Id})$ as a measure of the strength of the magnetic dipolar interactions in the system.[69] IF decreases passing from MagNPs to PHC and then to PLC (Table 2).

In fine particle systems, the IF parameter was observed to increase roughly linearly with increasing the packing density.[70] Similarly, we may expect that IF varies linearly with the concentration of nanoparticles in our samples, but it is easy to realize that this is not the case. Obviously, our samples cannot be modeled as a continuous matrix in which the magnetic nanoparticles are

homogeneously dispersed with a controllable packing density. As revealed by the TEM analysis (Figure 2), the magnetic nanoparticles form aggregates into the PLGA nanocapsules.

In order to minimize the magnetostatic energy of the aggregate as a whole, the dipolar interacting moments of the nanoparticles arrange in flux-closure configurations.[48, 49, 71] A better closure of the stray magnetic field is expected in larger aggregates, which therefore will be highly stable against the magnetizing action of the external field.[72] In our case, larger aggregates are observed by TEM in PHC rather than in PLC (Figure 2). The larger IF of PHC, compared to that of PLC, mainly reflects the higher H_{C_Ir}, since H_{C_Id} is almost similar in the two samples (Table 2). The higher H_{C_Ir} indicates a more difficult magnetizing process, i.e. it is consistent with the better stability of the aggregates in PHC.

In short, we conclude that the larger IF measured in PHC is related to the existence of aggregates of nanoparticles of larger size. The formation of aggregates realizing a better closure of the stray field in PHC is also supported by the lower squareness measured in this sample with respect to that found in PLC (Table 1). In this view, the MagNPs sample may be considered a limit case, corresponding to the 'infinite' aggregate.

It is quite well established that, given an assembly of magnetic nanoparticles, the effect of dipolar interactions can be taken into account considering that the nanoparticles are subjected to an effective magnetic anisotropy higher than the anisotropy that operates when they are isolated.[50, 52, 73]

To estimate the effective anisotropy coefficient K_{eff}, we consider the irreversibility magnetic field H_{irr} at T = 5 K (Table 2) – i.e., the field at which the descending and ascending branches of the hysteresis loop join up - as a measure of the anisotropy field of the system, namely $H_{irr} = 2K_{eff}/M_S$, where M_S is the saturation magnetization of the nanoparticles.[52, 74] We consider that M_S corresponds to the value of M_{50kOe} at T = 5 K of MagNPs, corrected for the presence of oleate, i.e. (86.7 ± 1.7) emu/g. To express it in (emu/cm^3), the value is multiplied by the density of the nanoparticles, assumed equal to that of bulk magnetite (5.1 g/cm^3).

The values of K_{eff} for MagNPs, PHC and PLC are reported in Table 2. We must point out that, due to the random orientation of the anisotropy axes of the nanoparticles with respect to the direction of the measuring field, H_{irr} is expected to be smaller than the anisotropy field, actually. Therefore, the obtained K_{eff} values are underestimated. However, in all the samples, K_{eff} is larger than the nominal magnetocrystalline anisotropy for bulk Fe_3O_4 (1.1×10^5 erg/cm^3), in spite of the Mn doping, which should rather decrease the anisotropy compared to pure magnetite.[56] The value calculated for MagNPs is the largest of the three, which is consistent with the overall state of strongest magnetic interactions and with the highest IF.

On the other hand, a similar K_{eff} is found in PHC and PLC, which may appear in contradiction with the different IF values measured in these two samples. It has been reported that the magnetization process in systems of interacting nanoparticles forming magnetic aggregates, as in PHC and PLC, takes place on two different length scales.[66, 75, 76] On a longer scale, the reorientation of the net magnetization vectors of the aggregates takes place; on a finer scale, the full alignment of the moments of the nanoparticles occurs. The first process is more difficult in the case of larger aggregates in which the interparticle dipolar interactions establish more efficient flux-closure configurations, as already argued in relation to the different values of IF in PHC and PLC. However, in general, we can schematically consider that the first process requires a lower magnetic field, whereas a higher field is needed to align the moments of the individual nanoparticles.[66, 75] The value of K_{eff} obtained for PHC and PLC from the measurement of H_{irr} is to be considered as an average value of the effective anisotropy that acts on the single nanoparticle during this second process. Since it is similar in the two samples, we conclude that it is not substantially affected by the size of the aggregates. Rather, K_{eff} may be related to the average interparticle distance within the aggregates, which seems similar in the TEM images of PHC and PLC (Figure 2b-e).

Information on the magnetic relaxing behavior of the samples is obtained by measuring the magnetization M as a function of T (from 5 to 300 K; heating rate 3 K/min) in a static magnetic field H_{appl} = 20 Oe, after cooling the sample from room temperature down to T = 5 K without applied field (zero-field-cooling procedure, ZFC) and in presence of H_{appl} (field-cooling, FC). The curves are shown in Figure 5, as normalized to the value of M_{FC} at T = 5 K. The magnetic irreversibility (difference between the values of M_{FC} and M_{ZFC}) indicates that the magnetic moments of the nanoparticles undergo thermally induced relaxation processes, which may culminate in the phenomenon of superparamagnetism at the so-called blocking temperature, namely when the thermal energy overcomes the anisotropy energy barrier for the moment reversal.[50]

Given an assembly of non-interacting nanoparticles and assuming the existence of a volume distribution, the temperature corresponding to the peak of M_{ZFC} is usually taken as a sort of average blocking temperature $\langle T_B \rangle$. However, if dipolar interactions exist in the same assembly of nanoparticles, generally the peak of M_{ZFC} is shifted towards higher temperatures.[50, 73] Indeed, the observation of a peak in M_{ZFC} at a temperature significantly higher than the expected $\langle T_B \rangle$ is usually considered the proof of the presence of interparticle magnetic interactions. However, in this second case, the physical meaning of the M_{ZFC} peak is not fully elucidated.

In our samples, we observe that the temperature corresponding to the M_{ZFC} peak (indicated as T_P) increases passing from PLC to PHC and finally to MagNPs and is proportional to IF in the three

samples, as one can realize by plotting T_P vs. IF (inset of Figure 5). Hence, we can certainly affirm that T_P is influenced by the presence of magnetic dipolar interactions between the nanoparticles and we may add that T_P is sensitive to the size of the aggregates of nanoparticles.

In all the samples, the M_{ZFC} and M_{FC} branches are superposed at T = 300 K. This finding and the absence of magnetic hysteresis indicate that all the nanoparticles are superparamagnetic at room temperature and in the SQUID measurement condition, which is usually assumed to correspond to a characteristic measuring time t_m = 100 s (measurement frequency $f_m = 1/t_m$ = 0.01 Hz).

3.3.3 $1/T_1$ Nuclear Magnetic Resonance Dispersion (NMRD) profiles

Due to the low water solubility of the oleate-coated magnetic nanoparticles, the NMR relaxation rates of water protons can be measured only when they are embedded into the PLGA nanocapsules, as they can form stable suspensions in aqueous solutions. Then, information on the characteristics of the magnetic nanoparticles loaded into PLGA can be obtained by measuring the NMRD profiles, i.e. the proton longitudinal relaxation $1/T_1$ as a function of the external applied magnetic field strength (Figure 7). In order to compare profiles acquired in different conditions, the relaxation rates reported on the y-axis [r_{1p} (s^{-1} mM^{-1})] are normalized to the (Fe+Mn) concentration (measured by ICP-MS).

The overall shape of the curves is similar for the two samples and is typical of the proton relaxation induced by magnetic nanoparticles undergoing superparamagnetic relaxation.[77] In general, the water proton longitudinal relaxation arises from the dipolar interaction between the magnetic moment of water protons and the magnetic moment of the magnetic nanoparticles. At low magnetic field, the proton relaxation can be modulated by the superparamagnetic relaxation of the magnetic nanoparticles and by water diffusion. At high magnetic field, the magnetic moments of the magnetic nanoparticles are blocked along the magnetic field direction and the proton relaxation only depends on the water diffusion.[78, 79] Differences in the NMRD profiles are usually ascribed to different properties of the magnetic nanoparticles (size, anisotropy, saturation magnetization).

In the NMRD profiles of PHC and PLC (Figure 6), both the amplitude and the position of the r_{1p} peak at high field (~ 2 MHz) are very similar. The Proton Larmor Frequency corresponding to the maximum of the peak depends essentially on the translational correlation time of water, which is expressed by the relation $\tau_D = r^2/D$, where r is the distance of minimum approach of water molecules to the nanoparticles and D is the water diffusion coefficient. It is to be remarked that the nanoparticles, though confined in the PLGA nanocapsules and subjected to dipolar interactions, are not in intimate contact. Hence, the water molecules, which can relatively freely diffuse inside the

nanocapsules,[40, 80] can approach the individual magnetic nanoparticles. The fact that the r_{1p} peak position and intensity do not change in the two profiles indicates that the magnetic properties of the individual nanoparticles are similar in PHC and PLC, as expected.

Nevertheless, the two profiles differ at low field, i.e. for values of the proton Larmor frequency < 1 MHz, since a substantially smaller r_{1p} is measured in PHC. Although the water molecules are able to approach the individual magnetic nanoparticles, one can surmise that the arrangement of the nanoparticles in form of dipolar interacting aggregates may affect the proton relaxation phenomenon at low field. In particular, r_{1p} may be smaller in PHC due to the presence of larger aggregates, which realize a better closure of the stray magnetic field sensed by the water protons. The presence of the dipolar aggregates does not affect the high-field region of the NMRD profiles, since the nanoparticles magnetic moments align along the field direction and no flux-closure magnetic configuration exists. This low field effect of the dipolar interactions between the magnetic nanoparticles is an interesting phenomenon and will deserve further attention.

3.4 Magnetic heating capacity

To test the magnetic heating capacity, the samples are exposed for 900 s to an alternating magnetic field with amplitude H_{max} = 228 Oe (i.e. 18 kA/m) and frequency f_m = 245 kHz (at T ~ 300 K). These parameters fulfill the safety criterion to avoid detrimental effects on healthy tissues, which recommends that ($H_{max} \times f_m$) does not exceed 5×10^9 A/m s.[81]

For the heating measurement, the sample MagNPs is dispersed in n-octane at a concentration of 10 mg/mL and the test is carried out on 1 mL of solution. The use of an apolar solvent, such as octane, is aimed at obtaining a good colloidal dispersion of the oleate-coated magnetic nanoparticles.[45]

The temperature increase $\Delta T(t)$ vs time t is shown in Figure 7a, being $\Delta T(t) = T(t) - T(t=0s)$. After 900 s, ΔT ~ 42 °C. This demonstrates the good capacity of the produced magnetic nanoparticles to generate heat in the adopted experimental conditions.

The heating efficiency of PHC and PLC is measured on the samples in HBS buffer. In particular, 1 mL of solution is considered. With respect to the test on MagNPs, the solvent is different and obviously no PLGA is present in MagNPs. However, we are certainly allowed to directly compare the heating tests on PHC and PLC, which are shown in Figure 7b. The temperature increase attained after 900 s is ΔT ~ 7.3 °C in PHC and ΔT ~ 3.5 °C in PLC, clearly not proportional to the fraction of loaded magnetic nanoparticles.

To compare quantitatively the heating efficiency of the two samples, we can evaluate the Specific Absorption Rate (SAR) parameter from the heating curves in Figure 7b, through the initial slope method, using the relation [82]

$$SAR = \frac{C}{m_{NPs}} \cdot \frac{\Delta T}{\Delta t} \qquad (2)$$

In this relation, C is the heat capacity of the sample, ΔT is the temperature increment during the short time interval Δt in which heat losses are supposed negligible, m_{NPs} is the mass of the magnetic nanoparticles contained in 1 mL. The latter parameter is obtained by comparing the amount of (Fe+Mn) measured in 1 mL of PHC and PLC by ICP-MS with that measured in standard solutions of MagNPs. It is found out that m_{NPs} = (3.7 ± 0.2) mg/mL in PHC and m_{NPs} = (0.43± 0.04) mg/mL in PLC. It is interesting to note that the ratio between these two values of m_{NPs}, estimated by ICP-MS, is (8.6 ± 1.2) and the ratio between the weight fractions of magnetic nanoparticles in PHC and PLC, estimated through the magnetization measurements, is (7.4 ± 0.5). Hence, the two ratios are equal within the errors, which means that the results obtained by the two techniques are consistent.
For each sample, ΔT/Δt is calculated as the slope of the linear curve fitting the heating curve for t in the 20 - 120 s interval. We take the heat capacity C equal to that of water (4.18 J/K). This implies that the heat capacity of the PLGA nanocapsules with their magnetic load is supposed negligible compared to that of the fluid in which they are dispersed, although the magnetic nanoparticles, i.e. the heating agents, are primarily surrounded by PLGA. We make this simplification since we intend just to compare the heating efficiency of PHC and PLC. The SAR values are (18 ± 1) W/g for PHC and (68 ± 6) W/g for PLC, which confirms that the heating efficiency is higher in the sample with the lower concentration of magnetic nanoparticles.

The heat generated by magnetic nanoparticles exposed to an alternating magnetic field, during one cycle, is equal to the area of the resulting hysteresis loop. In fact, the SAR parameter can also be expressed as the product of this area and f_m.[62] In an assembly of magnetic nanoparticles dispersed in a fluid, two magnetization mechanisms may be active, namely the internal rotation of the moments inside the nanoparticles and the physical rotation of the nanoparticles so that their moments align with the field (Brownian motion).
Regarding the first one, the nanoparticles that, in the adopted measurements conditions, are in the full superparamagnetic state do not generate heat because they do not exhibit the magnetic hysteresis phenomenon.[62]

In the macrospin approximation, the superparamagnetic relaxation of the magnetic moment of a single-domain nanoparticle is governed by the Néel relaxation time:

$$\tau_N = 1/f_0 \exp(KV/k_BT) \quad (3)$$

where KV is the magnetic anisotropy energy barrier (K is the magnetic anisotropy coefficient and V the volume of the nanoparticle), k_B the Boltzmann constant and f_0 the frequency factor, usually taken as 10^9 s^{-1}.[83] Being t_m the measuring time characteristic of the used investigating technique, the transition between the superparamagnetic and blocked regimes occurs at $\tau_N = t_m$; for $\tau_N < t_m$ the nanoparticle's moment undergoes superparamagnetic relaxation, whereas it is blocked for $\tau_N > t_m$. It follows that the entrance into the superparamagnetic regime will be observed to occur at a higher temperature using a technique with a shorter t_m.

In the heating tests, $t_m = 1/f_m = 4 \times 10^{-6}$ s. Hence, putting $\tau_N = t_m$, we can calculate, for T = 300 K, the critical nanoparticle size D_{SP} separating the superparamagnetic and the blocked regimes.[52] To this end, in relation (3) we set K equal to K_{eff}, despite the latter has been estimated at T = 5 K, actually. Hence, we neglect a possible thermal decrease of K_{eff}. However, this effect may be offset by the fact that K_{eff} is likely to be underestimated, as discussed in Section 3.3.2. The result is D_{SP} = (11.8 ± 0.2) nm for PHC and D_{SP} = (12.0 ± 0.2) nm for PLC, i.e. is the same within the experimental error, in line with the similar value of K_{eff} in the two samples (Table 2).

For completeness, it is worth pointing out that K_{eff} measured in MagNPs in the form of ferrofluid – i.e., dispersed in n-octane for the heating test – is (2.7 ± 0.1) erg/cm^3. It is lower than K_{eff} measured in the dried sample (Table 2) due to the larger interdistance between the magnetic nanoparticles and, hence, to the lower degree of interparticle magnetic interaction (this does not occur in PHC and PLC since the nanoparticles are immobilized into the PLGA).[52] Accordingly, D_{SP} = (10.7 ± 0.2) nm for MagNPs in the form of ferrofluid.

Regarding the Brownian rotation, in PHC and PLC the magnetic nanoparticles are embedded in the PLGA and hence are not free to move. However, one may consider the rotation of the whole PLGA nanocapsules, which, due to their magnetic load, can possibly bear a net magnetic moment. The Brownian relaxation is governed by the time $\tau_B = 3\eta V_H/k_BT$, where V_H is the hydrodynamic volume - which can be taken as $(D_{hyd})^3$, using the DLS results - and η is the viscosity of the fluid, assumed equal to that of water for the present case (0.01 P). For PHC and PLC, τ_B is of the order of 10^{-3} s, namely $\tau_B > t_m$, which means that the PLGA nanocapsules are fully thermally stable in the fluid, in the adopted experimental conditions.

In a previous work, we demonstrated that in ferrofluids obtained by dispersing Mn-doped magnetite nanoparticles in n-octane, the heating mechanism, probed using the same alternating field as in the present case, was sustained by the fraction of nanoparticles that were blocked with regard to both the Néel and the Brown relaxation.[52] In fact, the measurements were carried out in the regime of non-linear magnetic response, corresponding to the condition $\zeta = M_S V H_{max}/k_B T > 1$.[62] Also in the present case, the nanoparticles with $D > D_{SP}$, are blocked with regard to the Néel and the Brown relaxation, as just discussed. As for the ζ parameter in the tests on PHC and PLC, taking M_S equal to the value of M_{50kOe} at T = 300 K for MagNPs (Table 1) and $V = (D_{SP})^3$, we obtain $\zeta \sim 3$, which means that we are operating in the non-linear magnetic regime. The fraction of blocked nanoparticles in PHC and PLC, i.e. with size $D > D_{SP}$, can be estimated considering the size distribution in Figure 1b. Since D_{SP} is equal for PHC and PLC, we obtain that the fraction of nanoparticles effective in the heating mechanism is the same in the two samples, i.e. ~ 7 %. In terms of volume fraction, the blocked nanoparticles are ~ 22%. It is to be noticed that if the nominal K of bulk magnetite (1.1×10^5 erg/cm^3) were inserted in relation (3), instead of $K_{eff,}$ to calculate D_{SP}, we would obtain $D_{SP} \sim 14$ nm. However, the size of the nanoparticles in MagNPs, and hence also in PHC and PLC, is smaller than 14 nm (Figure 1b). Hence, we should conclude that there are no blocked nanoparticles, i.e. nanoparticles able to heat. This demonstrates the crucial role of dipolar interactions, which, increasing the effective magnetic anisotropy of the nanoparticles with respect to the intrinsic one, stabilize the magnetic moments against thermal effects.

However, this does not yet explain the different heating efficiency of the magnetic nanoparticles in the two PLGA samples. To address this point, once again we must consider the arrangement of the nanoparticles in form of aggregates and the role of the dipolar interactions. Although at T = 300 K, in the measurement conditions adopted in the heating tests, most magnetic nanoparticles are in the superparamagnetic state, the magnetic configuration of the aggregates is still determined by the need of reducing the magnetostatic energy, similarly to what we have demonstrated to occur at T = 5 K and as suggested by the room temperature analysis of the NMRD profiles. It should be considered that also superparamagnetic nanoparticles may be active in determining the equilibrium state of an assembly of dipolar interacting nanoparticles provided that the relaxation time characterizing the moment-moment interactions is smaller than the Néel relaxation time.[84]

Hence, a better stray field closure is attained in the large aggregates of PHC, which therefore are more stable against magnetization compared to those in PLC. Therefore, the hysteresis loop tracked by the alternating field during the heating measurement is expected to exhibit lower susceptibility

and lower remanence in sample PHC. This implies a smaller area of the loop measured in PHC compared to that of PLC and therefore a lower SAR, as observed.

This conclusion is in agreement with numerical simulations of hysteresis loops for systems of nanoparticles at different concentrations, showing a decrease in the magnetic susceptibility and remanence on increasing the concentration and, hence, the interparticle dipolar interactions.[51, 85, 86] Compared to those theoretical studies, we correlate the loop area, and hence the SAR parameter, not just to the concentration of nanoparticles, but more precisely to the size of the aggregates confined into the PLGA nanocapsules.

Conclusions

We have studied the structural and magnetic properties of two samples, PHC and PLC, consisting of PLGA nanocapsules (typical dimension around 200 nm) loaded with a different amount of oleate-coated Mn-doped magnetite nanoparticles (mean size ~ 8.4 nm). The content of magnetic nanoparticles, as estimated by magnetization measurements, is ~ 5.30 wt. % and ~ 0.72 wt. % for PHC and PLC, respectively. The TEM observations have revealed that the nanoparticles do not distribute homogeneously into the nanocapsules and tend to form aggregates, which are larger in sample PHC. The interparticle dipolar magnetic interactions rule the magnetic properties of the two samples, as revealed, in particular, by the analysis of the remanence curves at T = 5 K.

We have considered that the first step of the magnetization process, consisting in the reorientation of the magnetization vector of the aggregates, is more difficult in the case of larger aggregates, which realize a better flux-closure magnetic configuration. We have related the value of the effective interaction field IF – higher in PHC with respect to that found in PLC - to this process and therefore, ultimately, to the different size of the nanoparticle aggregates in the two samples. Conversely, the second magnetization step, corresponding to the alignment of the magnetic moments of the individual nanoparticles, is not affected by the size of the aggregates. In fact, the effective anisotropy K_{eff}, obtained from the measurement of the irreversibility field H_{irr} at T = 5 K, is larger than that of bulk magnetite due to the dipolar interacting state of the nanoparticles, but equal in both samples. This description is also consistent with the NMRD profiles measured at T = 25 °C on the two samples. In fact, while at low magnetic field the more efficient flux-closure configuration of the large aggregates in PHC reduces the magnetic field felt by solvent water protons and thus the magnetic relaxation, the position of the r_{1p} peaks at high field is very similar in PHC and PLC, indicating similar properties of the individual magnetic nanoparticles.

Thus, the different concentration of magnetic nanoparticles and the circumstance of being confined into the PLGA nanocapsules determine their spatial arrangement, the way in which they interact magnetically and their magnetic relaxing behavior as well as the size of the aggregates and their magnetic configuration.

These elements govern the magnetization process at T = 5 K, but we infer that they must also be determinant in the magnetization process at T = 300 K, temperature at which the heating tests have been carried out. A lower SAR is measured in PHC, which is the sample with the highest nanoparticle load. This has been accounted for considering that, in the heating tests, the larger aggregates of nanoparticles existing in PHC, more stable against magnetization, give rise to hysteresis loops of smaller area.

Hence, the double role of the dipolar interactions in the heating mechanism of the investigated system has been highlighted. On the one end, they are crucial for enhancing K_{eff}, thus stabilizing the nanoparticle magnetic moments with regard to the superparamagnetic relaxation and increasing the fraction of nanoparticles that are efficient in the heating mechanism. On the other hand, they give rise to low-remanence flux-closure magnetic configurations of the nanoparticle aggregates, which are detrimental for the heat generation. Therefore, in order to produce nanocarriers loaded with magnetic nanoparticles with high heating performance for biomedical applications, one should control and balance these two competing effects.

Supporting information

Characterization measurements on sample MagNPs: XRD, FT-IR, TGA (with and without magnetic field gradient). DLS analysis on samples PHC and PLC. Magnetization vs. T for the reference sample $PLGA_{Ref}$.

Acknowledgments

This work has been partially supported by a grant “Investimento Strategico di Dipartimento - SID” of the Department of Industrial Engineering, Padova University (Progetto SGAR_SID17_01).

Dr. Federico Caicci (Department of Biology, Padova University) is acknowledged for assistance in some TEM analyses. Prof. Michele Forzan (Department of Industrial Engineering, Padova University) is acknowledged for collaboration in the magnetic heating tests.

Table 1. The data refer to the samples labeled as indicated in Column 1. Columns 2 and 3: Magnetization $M_{50kOe,}$ measured at H = 50 kOe, at T = 5 K and 300 K, respectively. For sample MagNPs, in addition to the values of M_{50kOe} obtained by normalizing the magnetic moment to the whole sample mass (including 15 wt.% of oleate), the values calculated excluding the mass of oleate are reported. Column 4: Weight fraction of MagNPs in the samples. Obviously, this fraction corresponds to the whole sample in the case of MagNPs. Column 5: squareness M_r/ M^*_{50kOe} at T = 5 K; M_r is the remanent magnetization and M^*_{50kOe} is the calculated contribution of the magnetic nanoparticles only to the magnetization at T = 5 K (for MagNPs, M_{50kOe} and M^*_{50kOe} coincide). Column 6: coercivity H_C at T = 5 K.

Sample	M_{50kOe} at T = 5 K (emu/g)	M_{50kOe} at T = 300 K (emu/g)	MagNPs (wt.%)	M_r/M^*_{50kOe} at T = 5 K	H_C (Oe) at T = 5 K
MagNPs	73.7 ± 0.7 *(including oleate)* 86.7 ± 1.7 *(excluding oleate)*	58.2 ± 0.6 *(including oleate)* 68.5 ± 1.4 *(excluding oleate)*	100	0.15 ± 0.01	191 ± 3
PHC	3.96 ± 0.01	3.09 ± 0.01	5.3 ± 0.2	0.30 ± 0.02	177 ± 3
PLC	0.62 ± 0.01	0.42 ± 0.01	0.72 ± 0.03	0.37 ± 0.02	186 ± 3

Table 2. The data refer to the samples labeled as indicated in Column 1. Columns 2, 3 and 4: isothermal remanence coercivity $H_{C\_Ir,}$ demagnetization remanence coercivity H_{C_Id} and effective interaction field IF, respectively (T = 5 K). Columns 5 and 6: irreversibility field H_{irr} at T = 5 K and effective magnetic anisotropy K_{eff}.

Sample	H_{C_Ir} (Oe) ± 3 Oe	H_{C_Id} (Oe) ± 3 Oe	IF (Oe) ± 6 Oe	H_{irr} (Oe) ± 2%	K_{eff} (10^5 erg/cm^3) (± 0.1)
MagNPs	680	438	242	1200	3.9
PHC	409	309	100	930	2.0
PLC	350	297	53	880	1.9

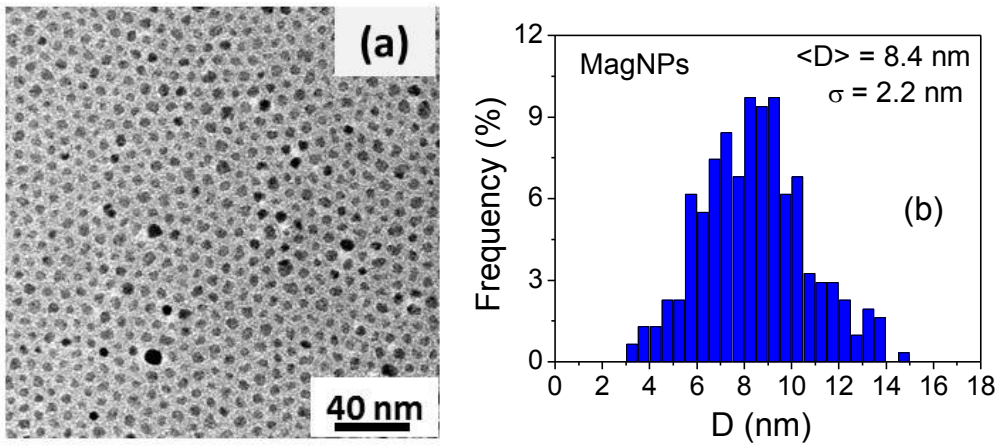

Figure 1. Typical TEM image (a) and size distribution (b) of the Mn-doped magnetite nanoparticles (sample MagNPs).

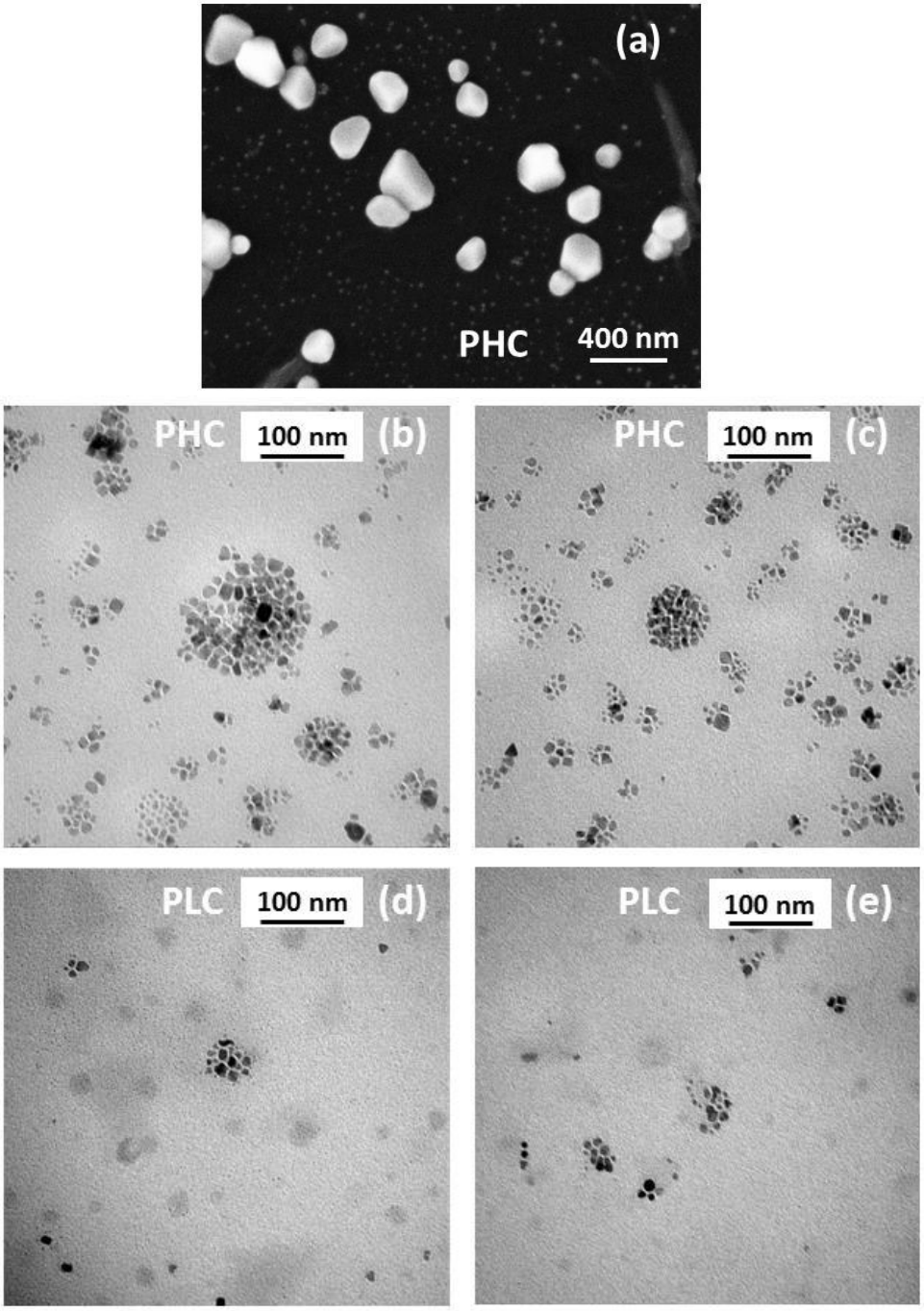

Figure 2. SEM image of sample PHC (a). Bright field TEM images of sample PHC (b-c) and sample PLC (d-e).

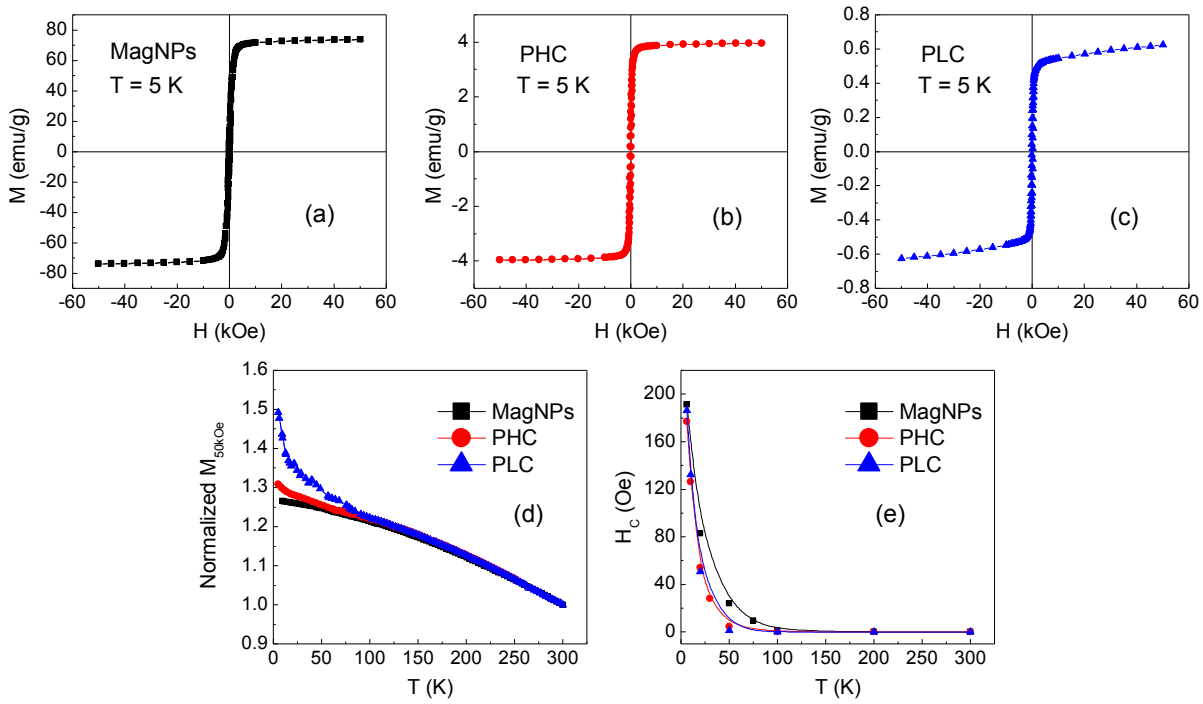

Figure 3. Magnetic hysteresis loops measured at T = 5 K on the samples in the dried form: (a) MagNPs, (b) PHC and (c) PLC. (d) Curves of magnetization (M_{50kOe}) vs. temperature (T) measured on MagNPs, PHC and PLC in H = 50 kOe, normalized to their values at T = 300 K. (e) Curves of the coercivity H_C vs. T for the three samples.

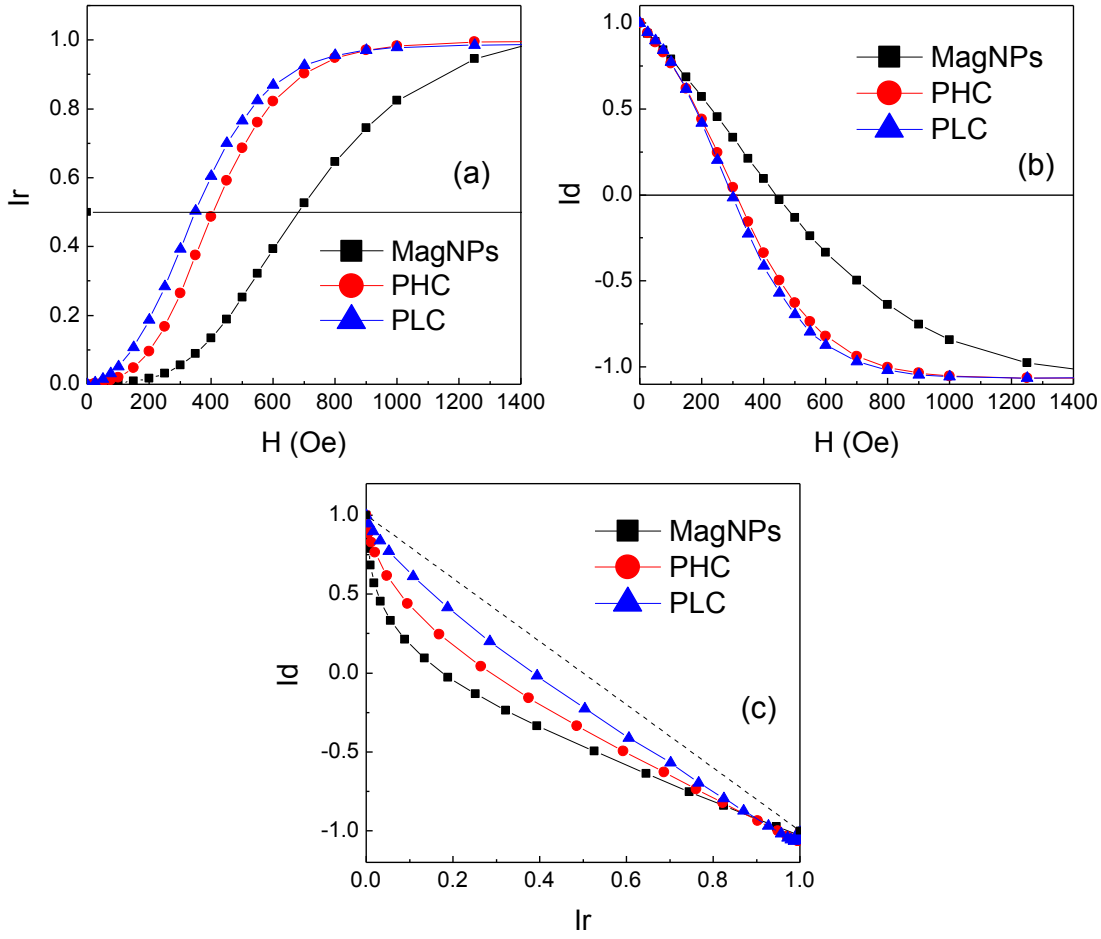

Figure 4. Magnetic remanence curves measured at T = 5 K on MagNPs, PHC and PLC: (a) Ir curves, from which one can derive the isothermal remanence coercivity H_{C_Ir}, which corresponds to the field at which Ir = 0.5; (b) Id curves, from which one can derive the demagnetization remanence coercivity H_{C_Id}, which is the field at which Id = 0. (c) Henkel plots for the three samples (T = 5 K). The dotted line is the linear Henkel plot expected for non-interacting nanoparticles.

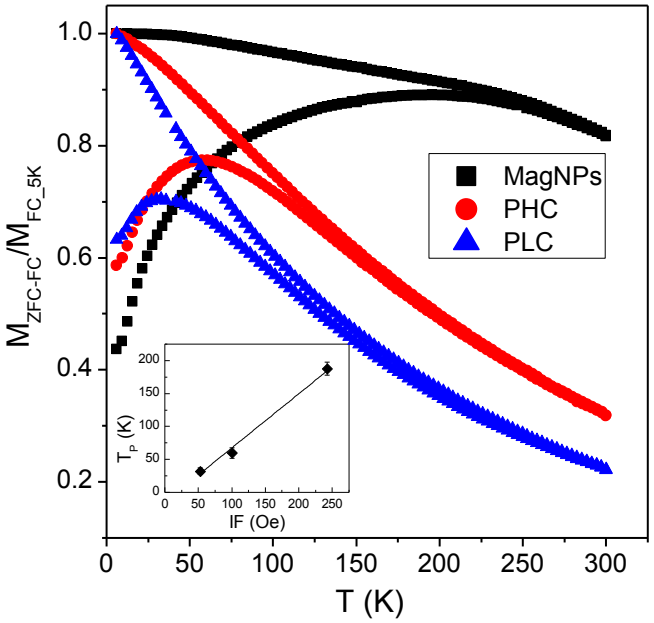

Figure 5. Magnetization measured on MagNPs, PHC and PLC for increasing temperature at H_{appl} = 20 Oe, after zero-field-cooling (M_{ZFC}, lower branch of each displayed curve) and after field-cooling (M_{FC}, upper branch). The curves are normalized to the value of M_{FC} at T = 5 K. Inset: Peak temperature of M_{ZFC} (T_P) shown as a function of the parameter IF (effective interaction field).

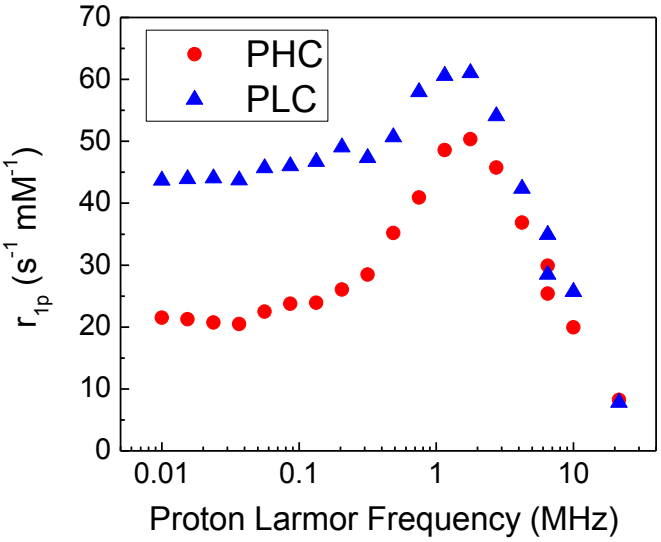

Figure 6. $1/T_1$ NMRD profiles of samples PHC and PLC measured at T = 25°C. The relaxation rates reported on the y-axis [r_{1p} (s^{-1} mM^{-1})] are normalized to the (Fe+Mn) concentration (measured by ICP-MS). The relaxation rate of HBS without nanoparticles is between 0.42-0.35 s^{-1} in the entire range of frequencies.

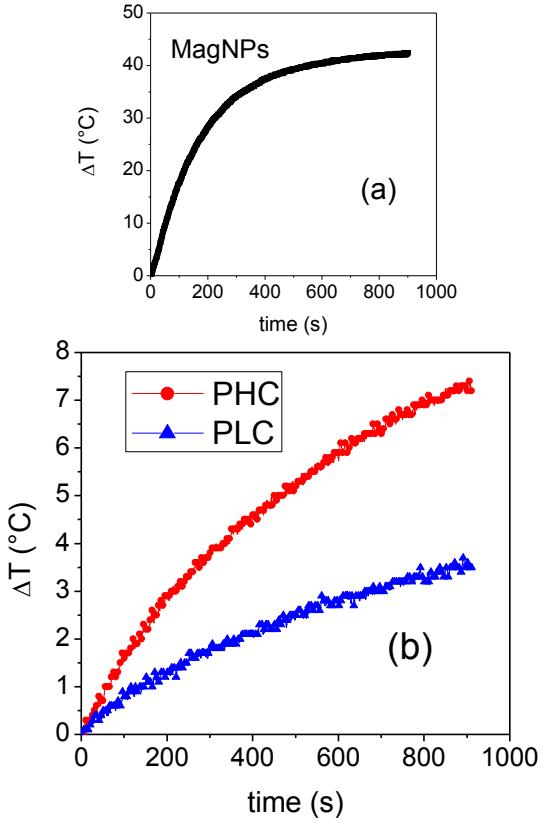

Figure 7. (a) Heating curves for the Mn-doped magnetite nanoparticles (sample MagNPs) dispersed in n-octane, measured in an alternating magnetic field of amplitude H_{max} = 228 Oe (i.e. 18 kA/m) and frequency f_m = 245 kHz. The temperature increase ΔT vs. time is plotted. (b) Heating curves for samples PHC and PLC in HBS buffer, measured in the same alternating field used for MagNPs.

References

(1) McCarthy, J. R.; Weissleder, R. Multifunctional Magnetic Nanoparticles for Targeted Imaging and Therapy. *Adv. Drug Deliv. Rev.* 2008, 60 (11), 1241–1251. https://doi.org/10.1016/j.addr.2008.03.014.

(2) Schladt, T. D.; Schneider, K.; Schild, H.; Tremel, W. Synthesis and Bio-Functionalization of Magnetic Nanoparticles for Medical Diagnosis and Treatment. *Dalton Trans.* 2011, *40* (24), 6315–6343. https://doi.org/10.1039/c0dt00689k.

(3) Thorat, N. D.; Townely, H.; Brennan, G.; Parchur, A. K.; Silien, C.; Bauer, J.; Tofail, S. A. M. Progress in Remotely Triggered Hybrid Nanostructures for Next-Generation Brain Cancer Theranostics. *ACS Biomater. Sci. Eng.* 2019, *5* (6), 2669–2687. https://doi.org/10.1021/acsbiomaterials.8b01173.

(4) Ashokan, A.; Somasundaram, V. H.; Gowd, G. S.; Anna, I. M.; Malarvizhi, G. L.; Sridharan, B.; Jobanputra, R. B.; Peethambaran, R.; Unni, A. K. K.; Nair, S.; et al. Biomineral Nano-Theranostic Agent for Magnetic Resonance Image Guided, Augmented Radiofrequency Ablation of Liver Tumor. *Sci. Rep.* 2017, *7* (1), 14481. https://doi.org/10.1038/s41598-017-14976-8.

(5) Bauer, L. M.; Situ, S. F.; Griswold, M. A.; Samia, A. C. S. High-Performance Iron Oxide Nanoparticles for Magnetic Particle Imaging – Guided Hyperthermia (HMPI). *Nanoscale* 2016, *8* (24), 12162–12169. https://doi.org/10.1039/C6NR01877G.

(6) Périgo, E. A.; Hemery, G.; Sandre, O.; Ortega, D.; Garaio, E.; Plazaola, F.; Teran, F. J. Fundamentals and Advances in Magnetic Hyperthermia. *Appl. Phys. Rev.* 2015, *2* (4), 041302. https://doi.org/10.1063/1.4935688.

(7) Lartigue, L.; Hugounenq, P.; Alloyeau, D.; Clarke, S. P.; Lévy, M.; Bacri, J.-C.; Bazzi, R.; Brougham, D. F.; Wilhelm, C.; Gazeau, F. Cooperative Organization in Iron Oxide Multi-Core Nanoparticles Potentiates Their Efficiency as Heating Mediators and MRI Contrast Agents. *ACS Nano* 2012, *6* (12), 10935–10949. https://doi.org/10.1021/nn304477s.

(8) Wu, W.; Jiang, C. Z.; Roy, V. A. L. Designed Synthesis and Surface Engineering Strategies of Magnetic Iron Oxide Nanoparticles for Biomedical Applications. *Nanoscale* 2016, *8* (47), 19421–19474. https://doi.org/10.1039/C6NR07542H.

(9) Furlani, E. P. Magnetic Biotransport: Analysis and Applications. *Materials* 2010, *3* (4), 2412–2446. https://doi.org/10.3390/ma3042412.

(10) McBain, S. C.; Yiu, H. HP.; Dobson, J. Magnetic nanoparticles for gene and drug delivery. *International Journal of Nanomedicine* 2008, *3* (2), 169–180. https://doi.org/10.2147/IJN.S1608.

(11) Khanna, L.; Verma, N. K.; Tripathi, S. K. Burgeoning Tool of Biomedical Applications - Superparamagnetic Nanoparticles. *J. Alloys Compd.* 2018, *752*, 332–353. https://doi.org/10.1016/j.jallcom.2018.04.093.

(12) Gawali, S. L.; Barick, B. K.; Barick, K. C.; Hassan, P. A. Effect of Sugar Alcohol on Colloidal Stabilization of Magnetic Nanoparticles for Hyperthermia and Drug Delivery Applications. *J. Alloys Compd.* 2017, *725*, 800–806. https://doi.org/10.1016/j.jallcom.2017.07.206.

(13) Lai, K.; Jiang, W.; Tang, J. Z.; Wu, Y.; He, B.; Wang, G.; Gu, Z. Superparamagnetic Nano-Composite Scaffolds for Promoting Bone Cell Proliferation and Defect Reparation without a Magnetic Field. *RSC Adv.* 2012, *2* (33), 13007−13017. https://doi.org/10.1039/c2ra22376g.

(14) Yang, X.; Grailer, J. J.; Pilla, S.; Steeber, D. A.; Gong, S. Tumor-Targeting, PH-Responsive, and Stable Unimolecular Micelles as Drug Nanocarriers for Targeted Cancer Therapy. *Bioconjug. Chem.* 2010, *21* (3), 496–504. https://doi.org/10.1021/bc900422j.

(15) Sahoo, B.; Devi, K. S. P.; Banerjee, R.; Maiti, T. K.; Pramanik, P.; Dhara, D. Thermal and PH Responsive Polymer-Tethered Multifunctional Magnetic Nanoparticles for Targeted Delivery of Anticancer Drug. *ACS Appl. Mater. Interfaces* 2013, *5* (9), 3884–3893. https://doi.org/10.1021/am400572b.

(16) Kurlyandskaya, G.; Litvinova, L.; Safronov, A.; Schupletsova, V.; Tyukova, I.; Khaziakhmatova, O.; Slepchenko, G.; Yurova, K.; Cherempey, E.; Kulesh, N.; et al. Water-Based Suspensions of Iron Oxide Nanoparticles with Electrostatic or Steric Stabilization by Chitosan: Fabrication, Characterization and Biocompatibility. *Sensors* 2017, *17* (11), 2605. https://doi.org/10.3390/s17112605.

(17) Puig, J.; Hoppe, C. E.; Fasce, L. A.; Pérez, C. J.; Piñeiro-Redondo, Y.; Bañobre-López, M.; López-Quintela, M. A.; Rivas, J.; Williams R. J. J. Superparamagnetic Nanocomposites Based on the Dispersion of Oleic Acid-Stabilized Magnetite Nanoparticles in a Diglycidylether of Bisphenol A-Based Epoxy Matrix: Magnetic Hyperthermia and Shape Memory. *J. Phys. Chem. C* 2012, *116* (24), 13421−13428. https://doi.org/10.1021/jp3026754.

(18) Chandra, S.; Nigam, S.; Bahadur, D. Combining Unique Properties of Dendrimers and Magnetic Nanoparticles Towards Cancer Theranostics. *J. Biomed. Nanotechnol.* 2014, *10* (1), 32–49. https://doi.org/10.1166/jbn.2014.1698.

(19) Thoniyot, P.; Tan, M. J.; Karim, A. A.; Young, D. J.; Loh, X. J. Nanoparticle-Hydrogel Composites: Concept, Design, and Applications of These Promising, Multi-Functional Materials. *Adv. Sci.* 2015, *2* (1–2), 1400010. https://doi.org/10.1002/advs.201400010.

(20) Xu, F.; Inci, F.; Mullick, O.; Gurkan, U. A.; Sung, Y.; Kavaz, D.; Li, B.; Denkbas, E. B.; Demirci, U. Release of Magnetic Nanoparticles from Cell-Encapsulating Biodegradable Nanobiomaterials. *ACS Nano* 2012, *6* (8), 6640–6649. https://doi.org/10.1021/nn300902w.

(21) Engelmann, U. M.; Seifert, J.; Mues, B.; Roitsch, S.; Menager, C.; Schmidt, A. M..; Slabu, I. Heating efficiency of magnetic nanoparticles decreases with gradual immobilization in hydrogels. *J. Magn. Magn. Mater.* 2019, *471*, 486–494. https://doi.org/10.1016/j.jmmm.2018.09.113

(22) de Alcântara Sica de Toledo, L.; Rosseto, H. C.; dos Santos, R. S.; Spizzo, F.; Del Bianco, L.; Montanha, M. C.; Esposito, E.; Kimura, E.; Bonfim-Mendonça, P. de S.; Svidzinski, T. I. E.; et al. Thermal Magnetic Field Activated Propolis Release From Liquid Crystalline System Based on Magnetic Nanoparticles. *AAPS PharmSciTech* 2018, *19* (7), 3258–3271. https://doi.org/10.1208/s12249-018-1163-4.

(23) Olsson, R. T.; Azizi Samir, M. A. S.; Salazar-Alvarez, G.; Belova, L.; Ström, V.; Berglund, L. A.; Ikkala, O.; Nogués, J.; Gedde, U. W. Making Flexible Magnetic Aerogels and Stiff Magnetic Nanopaper Using Cellulose Nanofibrils as Templates. *Nat. Nanotechnol.* 2010, *5* (8), 584–588. https://doi.org/10.1038/nnano.2010.155.

(24) Samal, S. K.; Dash, M.; Shelyakova, T.; Declercq, H. A.; Uhlarz, M.; Bañobre-López, M.; Dubruel, P.; Cornelissen, M.; Herrmannsdörfer, T.; Rivas, J.; et al. Biomimetic Magnetic Silk Scaffolds. *ACS Appl. Mater. Interfaces* 2015, *7* (11), 6282–6292. https://doi.org/10.1021/acsami.5b00529.

(25) Del Bianco, L.; Lesci, I. G.; Fracasso, G.; Barucca, G.; Spizzo, F.; Tamisari, M.; Scotti, R.; Ciocca, L. Synthesis of Nanogranular Fe 3 O 4 /Biomimetic Hydroxyapatite for Potential Applications in Nanomedicine: Structural and Magnetic Characterization. *Mater. Res. Express* 2015, *2* (6), 065002. https://doi.org/10.1088/2053-1591/2/6/065002.

(26) Derfus, A. M.; von Maltzahn, G.; Harris, T. J.; Duza, T.; Vecchio, K. S.; Ruoslahti, E.; Bhatia, S. N. Remotely Triggered Release from Magnetic Nanoparticles. *Adv. Mater.* 2007, *19* (22), 3932–3936. https://doi.org/10.1002/adma.200700091.

(27) Kumar, C. S. S. R.; Mohammad, F. Magnetic Nanomaterials for Hyperthermia-Based Therapy and Controlled Drug Delivery. *Adv. Drug Deliv. Rev.* 2011, *63* (9), 789–808. https://doi.org/10.1016/j.addr.2011.03.008.

(28) Zeng, X.; Zeng, X.; Hu; Xie; Lan; Wu; Jiang; Gu, Z. Magnetic Responsive Hydroxyapatite Composite Scaffolds Construction for Bone Defect Reparation. *Int. J. Nanomedicine* 2012, *7*, 3365−3378. https://doi.org/10.2147/IJN.S32264.

(29) Bock, N.; Riminucci, A.; Dionigi, C.; Russo, A.; Tampieri, A.; Landi, E.; Goranov, V. A.; Marcacci, M.; Dediu, V. A Novel Route in Bone Tissue Engineering: Magnetic Biomimetic Scaffolds. *Acta Biomater.* 2010, *6* (3), 786–796. https://doi.org/10.1016/j.actbio.2009.09.017.

(30) Fuhrer, R.; Athanassiou, E. K.; Luechinger, N. A.; Stark, W. J. Crosslinking Metal Nanoparticles into the Polymer Backbone of Hydrogels Enables Preparation of Soft, Magnetic Field-Driven Actuators with Muscle-Like Flexibility. *Small* 2009, *5* (3), 383–388. https://doi.org/10.1002/smll.200801091.

(31) Thiruvengadam, V.; Vitta, S. Ni–Bacterial Cellulose Nanocomposite; a Magnetically Active Inorganic–Organic Hybrid Gel. *RSC Adv.* 2013, *3* (31), 12765. https://doi.org/10.1039/c3ra40944a.

(32) Kim, J.; Lee, J. E.; Lee, S. H.; Yu, J. H.; Lee, J. H.; Park, T. G.; Hyeon, T. Designed Fabrication of a Multifunctional Polymer Nanomedical Platform for Simultaneous Cancer- Targeted Imaging and Magnetically Guided Drug Delivery. *Adv. Mater.* 2008, *20* (3), 478–483. https://doi.org/10.1002/adma.200701726.

(33) Abbasi, A. Z.; Gutiérrez, L.; del Mercato, L. L.; Herranz, F.; Chubykalo-Fesenko, O.; Veintemillas-Verdaguer, S.; Parak, W. J.; Morales, M. P.; González, J. M.; Hernando, A.; et al. Magnetic Capsules for NMR Imaging: Effect of Magnetic Nanoparticles Spatial Distribution and Aggregation. *J. Phys. Chem. C* 2011, *115* (14), 6257−6264. https://doi.org/10.1021/jp1118234.

(34) Arcos, D.; Fal-Miyar, V.; Ruiz-Hernández, E.; Garcia-Hernández, M.; Ruiz-González, M. L.; González-Calbet, J.; Vallet-Regí, M. Supramolecular Mechanisms in the Synthesis of Mesoporous Magnetic Nanospheres for Hyperthermia. *J. Mater. Chem.* 2012, *22* (1), 64–72. https://doi.org/10.1039/C1JM13102H.

(35) Rodrigues, A. R. O.; Almeida, B. G.; Rodrigues, J. M.; Queiroz, M. J. R. P.; Calhelha, R. C.; Ferreira, I. C. F. R.; Pires, A.; Pereira, A. M.; Araújo, J. P.; Coutinho, P. J. G.; et al. Magnetoliposomes as Carriers for Promising Antitumor Thieno[3,2-b]Pyridin-7-Arylamines: Photophysical and Biological Studies. *RSC Adv.* 2017, *7* (25), 15352–15361. https://doi.org/10.1039/C7RA00447H.

(36) Fortes Brollo, M. E.; Hernández Flores, P.; Gutiérrez, L.; Johansson, C.; Barber, D. F.; Morales, M. del P. Magnetic Properties of Nanoparticles as a Function of Their Spatial Distribution on Liposomes and Cells. *Phys. Chem. Chem. Phys.* 2018, *20* (26), 17829–17838. https://doi.org/10.1039/C8CP03016B.

(37) Slabu, I.; Roeth, A. A.; Engelmann, U. M.; Wiekhorst, F.; Buhl, E. M.; Neumann, U. P.; Schmitz-Rode, T. Modeling of Magnetoliposome Uptake in Human Pancreatic Tumor Cells in Vitro. *Nanotechnology* 2019, *30* (18), 184004. https://doi.org/10.1088/1361-6528/ab033e.

(38) Liu, X.; Kaminski, M. D.; Chen, H.; Torno, M.; Taylor, L.; Rosengart, A. J. Synthesis and Characterization of Highly-Magnetic Biodegradable Poly(d,l-Lactide-Co-Glycolide) Nanospheres. *J. Control. Release* 2007, *119* (1), 52–58. https://doi.org/10.1016/j.jconrel.2006.11.031.

(39) Wang, Y.; Ng, Y. W.; Chen, Y.; Shuter, B.; Yi, J.; Ding, J.; Wang, S. -c.; Feng, S. S. Formulation of Superparamagnetic Iron Oxides by Nanoparticles of Biodegradable Polymers for Magnetic Resonance Imaging. *Adv. Funct. Mater.* 2008, *18* (2), 308–318. https://doi.org/10.1002/adfm.200700456.

(40) Ruggiero, M. R.; Geninatti Crich, S.; Sieni, E.; Sgarbossa, P.; Forzan, M.; Cavallari, E.; Stefania, R.; Dughiero, F.; Aime, S. Magnetic Hyperthermia Efficiency and 1 H-NMR Relaxation Properties of Iron Oxide/Paclitaxel-Loaded PLGA Nanoparticles. *Nanotechnology* 2016, *27* (28), 285104. https://doi.org/10.1088/0957-4484/27/28/285104.

(41) Yang, J.; Lee, C.-H.; Park, J.; Seo, S.; Lim, E.-K.; Song, Y. J.; Suh, J.-S.; Yoon, H.-G.; Huh, Y.-M.; Haam, S. Antibody Conjugated Magnetic PLGA Nanoparticles for Diagnosis and Treatment of Breast Cancer. *J. Mater. Chem.* 2007, *17* (26), 2695–2699. https://doi.org/10.1039/b702538f.

(42) Jia, Y.; Yuan, M.; Yuan, H.; Huang, X.; Sui, X.; Cui, X.; Tang, F.; Peng, J.; Chen, J.; Lu, S.; et al. Co-encapsulation of magnetic Fe_3O_4 nanoparticles and doxorubicin into biodegradable PLGA nanocarriers for intratumoral drug delivery, *Int. J. Nanomedicine* 2012, *7*, 1697–1708. https://doi.org/10.2147/IJN.S28629

(43) Kapoor, D. N.; Bhatia, A.; Kaur, R.; Sharma, R.; Kaur, G.; Dhawan, S. PLGA: A Unique Polymer for Drug Delivery. *Ther. Deliv.* 2015, *6* (1), 41–58. https://doi.org/10.4155/tde.14.91.

(44) Danhier, F.; Ansorena, E.; Silva, J. M.; Coco, R.; Le Breton, A.; Préat, V. PLGA-Based Nanoparticles: An Overview of Biomedical Applications. *J. Control. Release* 2012, *161* (2), 505–522. https://doi.org/10.1016/j.jconrel.2012.01.043.

(45) Sun, S.; Zeng, H.; Robinson, D. B.; Raoux, S.; Rice, P. M.; Wang, S. X.; Li, G. Monodisperse MFe_2O_4 (M = Fe, Co, Mn) Nanoparticles. *J. Am. Chem. Soc.* 2004, *126* (1), 273–279. https://doi.org/10.1021/ja0380852.

(46) Roca, A. G.; Costo, R.; Rebolledo, A. F.; Veintemillas-Verdaguer, S.; Tartaj, P.; González-Carreño, T.; Morales, M. P.; Serna, C. J. Progress in the Preparation of Magnetic Nanoparticles for Applications in Biomedicine. *J. Phys. D. Appl. Phys.* 2009, *42* (22), 224002. https://doi.org/10.1088/0022-3727/42/22/224002.

(47) de la Presa, P.; Luengo, Y.; Velasco, V.; Morales, M. P.; Iglesias, M.; Veintemillas-Verdaguer, S.; Crespo, P.; Hernando, A. Particle Interactions in Liquid Magnetic Colloids by Zero Field Cooled Measurements: Effects on Heating Efficiency. *J. Phys. Chem. C* 2015**,** *119* (20), 11022-11030. https://doi.org/10.1021/jp5115515.

(48) Tripp, S. L.; Dunin-Borkowski, R. E.; Wei, A. Flux Closure in Self-Assembled Cobalt Nanoparticle Rings. *Angew. Chemie Int. Ed.* 2003, *42* (45), 5591–5593. https://doi.org/10.1002/anie.200352825.

(49) Spizzo, F.; Tamisari, M.; Chinni, F.; Bonfiglioli, E.; Gerardino, A.; Barucca, G.; Bisero, D.; Fin, S.; Del Bianco, L. Exchange Bias Properties of 140 Nm-Sized Dipolarly Interacting Circular Dots with Ultrafine IrMn and NiFe Layers. *J. Magn. Magn. Mater.* 2016, *400*, 242–247. https://doi.org/10.1016/j.jmmm.2015.08.001.

(50) Dormann, J. L.; Fiorani, D.; Tronc, E. Magnetic Relaxation in Fine-Particle Systems. In *Advances in Chemical Physics vol. XCVIII*; John Wiley & Sons, Inc.: New York, USA, 2007; pp 283–494. https://doi.org/10.1002/9780470141571.ch4.

(51) Mehdaoui, B.; Tan, R. P.; Meffre, A.; Carrey, J.; Lachaize, S.; Chaudret, B.; Respaud, M. Increase of Magnetic Hyperthermia Efficiency Due to Dipolar Interactions in Low-Anisotropy Magnetic Nanoparticles: Theoretical and Experimental Results. *Phys. Rev. B* 2013, *87* (17), 174419. https://doi.org/10.1103/PhysRevB.87.174419.

(52) Del Bianco, L.; Spizzo, F.; Barucca, G.; Ruggiero, M. R.; Geninatti Crich, S.; Forzan, M.; Sieni, E.; Sgarbossa, P. Mechanism of Magnetic Heating in Mn-Doped Magnetite Nanoparticles and the Role of Intertwined Structural and Magnetic Properties. *Nanoscale* 2019, *11* (22), 10896–10910. https://doi.org/10.1039/C9NR03131F.

(53) Serantes, D.; Simeonidis, K.; Angelakeris, M.; Chubykalo-Fesenko, O.; Marciello, M.; Morales, M. P.; Baldomir, D.; Martinez-Boubeta, C. Multiplying magnetic hyperthermia response by nanoparticle assembling. *J. Phys. Chem. C* 2014, *118* (11), 5927−5934. https://doi.org/10.1021/jp410717m.

(54) Salas, G.; Camarero, J.; Cabrera, D.; Takacs, H.; Varela, M.; Ludwig, R.; Dähring, H.; Hilger, I.; Miranda, R.; Morales, M. P.; et. al. Modulation of Magnetic Heating via Dipolar Magnetic Interactions in Monodisperse and Crystalline Iron Oxide Nanoparticles. *J. Phys. Chem. C* 2014, *118* (34), 19985-19994. https://doi.org/10.1021/jp5041234.

(55) Muela, A.; Muñoz, D.; Martín-Rodríguez, R.; Orue, I.; Garaio, E.; Cerio, A. A. D.; Alonso, J.; García, J. A′.; Fdez-Gubieda, M. L. Optimal Parameters for Hyperthermia Treatment Using

Biomineralized Magnetite Nanoparticles: Theoretical and Experimental Approach. *J. Phys. Chem. C* 2016, *120* (42), 24437−24148. https://doi.org/10.1021/acs.jpcc.6b07321.

(56) Giri, J.; Pradhan, P.; Sriharsha, T.; Bahadur, D. Preparation and Investigation of Potentiality of Different Soft Ferrites for Hyperthermia Applications. *J. Appl. Phys.* 2005, *97* (10), 10Q916. https://doi.org/10.1063/1.1855131.

(57) Lee, J.-H.; Jang, J.; Choi, J.; Moon, S. H.; Noh, S.; Kim, J.; Kim, J.-G.; Kim, I.-S.; Park, K. I.; Cheon, J. Exchange-Coupled Magnetic Nanoparticles for Efficient Heat Induction. *Nat. Nanotechnol.* 2011, *6* (7), 418–422. https://doi.org/10.1038/nnano.2011.95.

(58) Yang, L.; Ma, L.; Xin, J.; Li, A.; Sun, C.; Wei, R.; Ren, B. W.; Chen, Z.; Lin, H.; Gao, J. Composition Tunable Manganese Ferrite Nanoparticles for Optimized T_2 Contrast Ability. *Chem. Mater.* 2017, *29* (7), 3038–3047. https://doi.org/10.1021/acs.chemmater.7b00035.

(59) Coey, J. M. D. Noncollinear Spin Arrangement in Ultrafine Ferrimagnetic Crystallites. *Phys. Rev. Lett.* 1971, *27* (17), 1140–1142. https://doi.org/10.1103/PhysRevLett.27.1140.

(60) Parker, F. T.; Foster, M. W.; Margulies, D. T.; Berkowitz, A. E. Spin Canting, Surface Magnetization, And Finite-size Effects In γ-Fe_2O_3 Particles. *Phys. Rev. B* 1993, *47* (13), 7885–7891. https://doi.org/10.1103/PhysRevB.47.7885.

(61) Spizzo, F.; Sgarbossa, P.; Sieni, E.; Semenzato, A.; Dughiero, F.; Forzan, M.; Bertani, R.; Del Bianco, L. Synthesis of Ferrofluids Made of Iron Oxide Nanoflowers: Interplay between Carrier Fluid and Magnetic Properties. *Nanomaterials* 2017, *7* (11), 373. https://doi.org/10.3390/nano7110373.

(62) Carrey, J.; Mehdaoui, B.; Respaud, M. Simple Models for Dynamic Hysteresis Loop Calculations of Magnetic Single-Domain Nanoparticles: Application to Magnetic Hyperthermia Optimization. *J. Appl. Phys.* 2011, *109* (8), 083921. https://doi.org/10.1063/1.3551582.

(63) Zborowski, M.; Chalmers, J. J. Magnetophoresis: Fundamentals and Applications. In *Wiley Encyclopedia of Electrical and Electronics Engineering*; John Wiley & Sons, Inc.: Hoboken, NJ, USA, 2015; pp 1–23. https://doi.org/10.1002/047134608X.W8236.

(64) Zhang, H.; Li, L.; Liu, X. L.; Jiao, J.; Ng, C.-T.; Yi, J. B.; Luo, Y. E.; Bay, B.-H.; Zhao, L. Y.; Peng, M. L.; et al. Ultrasmall Ferrite Nanoparticles Synthesized via Dynamic Simultaneous Thermal Decomposition for High-Performance and Multifunctional T_1 Magnetic Resonance Imaging Contrast Agent. *ACS Nano* 2017, *11* (4), 3614–3631. https://doi.org/10.1021/acsnano.6b07684.

(65) Di Barba, P.; Dughiero, F.; Sieni, E. Magnetic Field Synthesis in the Design of Inductors for Magnetic Fluid Hyperthermia. *IEEE Trans. Magn.* 2010, *46* (8), 2931–2934. https://doi.org/10.1109/TMAG.2010.2044769.

(66) Del Bianco, L.; Spizzo, F.; Li, T.; Adhikari, R.; Bonanni, A. Influence of Mn Co-Doping on the Magnetic Properties of Planar Arrays of $Ga_xFe_{4-x}N$ Nanocrystals in a GaN Matrix. *Phys. Chem. Chem. Phys.* 2018, *20* (39), 25411–25420. https://doi.org/10.1039/C8CP04475A.

(67) Wohlfarth, E. P. Relations between Different Modes of Acquisition of the Remanent Magnetization of Ferromagnetic Particles. *J. Appl. Phys.* 1958, *29* (3), 595–596. https://doi.org/10.1063/1.1723232.

(68) Henkel, O. Remanenzverhalten Und Wechselwirkungen in Hartmagnetischen Teilchenkollektiven. *Phys. status solidi* 1964, *7* (3), 919–929. https://doi.org/10.1002/pssb.19640070320.

(69) Fearon, M.; Chantrell, R. W.; Wohlfarth, E. P. A Theoretical Study of Interaction Effects on the Remanence Curves of Particulate Dispersions. *J. Magn. Magn. Mater.* 1990, *86* (2–3), 197–206. https://doi.org/10.1016/0304-8853(90)90121-6.

(70) Corradi, A.; Wohlfarth, E. Influence of Densification on the Remanence, the Coercivities and the Interaction Field of Elongated γFe_20_3 Powders. *IEEE Trans. Magn.* 1978, *14* (5), 861–863. https://doi.org/10.1109/TMAG.1978.1059788.

(71) Georgescu, M.; Klokkenburg, M.; Erné, B. H.; Liljeroth, P.; Vanmaekelbergh, D.; Zeijlmans van Emmichoven, P. A. Flux Closure in Two-Dimensional Magnetite Nanoparticle Assemblies. *Phys. Rev. B* 2006, *73* (18), 184415. https://doi.org/10.1103/PhysRevB.73.184415.

(72) Chantrell, R. W.; Walmsley, N.; Gore, J.; Maylin, M. Calculations of the Susceptibility of Interacting Superparamagnetic Particles. *Phys. Rev. B* 2000, *63* (2), 024410. https://doi.org/10.1103/PhysRevB.63.024410.

(73) Del Bianco, L.; Fiorani, D.; Testa, A. M.; Bonetti, E.; Savini, L.; Signoretti, S. Magnetothermal Behavior of a Nanoscale Fe/Fe Oxide Granular System. *Phys. Rev. B* 2002, *66* (17), 174418. https://doi.org/10.1103/PhysRevB.66.174418.

(74) Fiorani, D.; Testa, A. M.; Lucari, F.; D'Orazio, F.; Romero, H. Magnetic Properties of Maghemite Nanoparticle Systems: Surface Anisotropy and Interparticle Interaction Effects. *Phys. B Condens. Matter* 2002, *320* (1–4), 122–126. https://doi.org/10.1016/S0921-4526(02)00659-2.

(75) Allia, P.; Coisson, M.; Spizzo, F.; Tiberto, P.; Vinai, F. Magnetic Correlation States in Cosputtered Granular $Ag_{100-x}Fe_x$ Films. *Phys. Rev. B* 2006, *73* (5), 054409. https://doi.org/10.1103/PhysRevB.73.054409.

(76) Del Bianco, L.; Spizzo, F.; Tamisari, M.; Calbucci, M.; Allia, P. Study of the Magnetic Microstructure of Ni/NiO Nanogranular Samples above the Electric Percolation Threshold by Magnetoresistance Measurements. *J. Phys. Condens. Matter* 2012, *24* (30), 306004. https://doi.org/10.1088/0953-8984/24/30/306004.

(77) Laurent, S.; Forge, D.; Port, M.; Roch, A.; Robic, C.; Vander Elst, L.; Muller, R. N. Magnetic Iron Oxide Nanoparticles: Synthesis, Stabilization, Vectorization, Physicochemical Characterizations, and Biological Applications. *Chem. Rev.* 2008, *108* (6), 2064–2110. https://doi.org/10.1021/cr068445e.

(78) Bordonali, L.; Kalaivani, T.; Sabareesh, K. P. V; Innocenti, C.; Fantechi, E.; Sangregorio, C.; Casula, M. F.; Lartigue, L.; Larionova, J.; Guari, Y.; et al. NMR-D Study of the Local Spin Dynamics and Magnetic Anisotropy in Different Nearly Monodispersed Ferrite Nanoparticles. *J. Phys. Condens. Matter* 2013, *25* (6), 066008. https://doi.org/10.1088/0953-8984/25/6/066008.

(79) Roch, A.; Muller, R. N.; Gillis, P. Theory of Proton Relaxation Induced by Superparamagnetic Particles. *J. Chem. Phys.* 1999, *110* (11), 5403–5411. https://doi.org/10.1063/1.478435.

(80) Mariano, R. N.; Alberti, D.; Cutrin, J. C.; Geninatti Crich, S.; Aime, S. Design of PLGA Based Nanoparticles for Imaging Guided Applications. *Mol. Pharm.* 2014, *11* (11), 4100–4106. https://doi.org/10.1021/mp5002747.

(81) Hergt, R.; Dutz, S. Magnetic Particle Hyperthermia—Biophysical Limitations of a Visionary Tumour Therapy. *J. Magn. Magn. Mater.* 2007, *311* (1), 187–192. https://doi.org/10.1016/j.jmmm.2006.10.1156.

(82) Andreu, I.; Natividad, E. Accuracy of Available Methods for Quantifying the Heat Power Generation of Nanoparticles for Magnetic Hyperthermia. *Int. J. Hyperth.* 2013, *29* (8), 739–751. https://doi.org/10.3109/02656736.2013.826825.

(83) Blanco-Mantecón, M.; O'Grady, K. Interaction and Size Effects in Magnetic Nanoparticles. *J. Magn. Magn. Mater.* 2006, *296* (2), 124–133. https://doi.org/10.1016/j.jmmm.2004.11.580.

(84) Allia, P.; Coisson, M.; Knobel, M.; Tiberto, P.; Vinai, F. Magnetic Hysteresis Based on Dipolar Interactions in Granular Magnetic Systems. *Phys. Rev. B* 1999, *60* (17), 12207–12218. https://doi.org/10.1103/PhysRevB.60.12207.

(85) Haase, C.; Nowak, U. Role of Dipole-Dipole Interactions for Hyperthermia Heating of Magnetic Nanoparticle Ensembles. *Phys. Rev. B* 2012, *85* (4), 045435. https://doi.org/10.1103/PhysRevB.85.045435.

(86) Serantes, D.; Baldomir, D.; Martinez-Boubeta, C.; Simeonidis, K.; Angelakeris, M.; Natividad, E.; Castro, M.; Mediano, A.; Chen, D.-X.; Sanchez, A.; et al. Influence of Dipolar Interactions on Hyperthermia Properties of Ferromagnetic Particles. *J. Appl. Phys.* 2010, *108* (7), 073918. https://doi.org/10.1063/1.3488881.

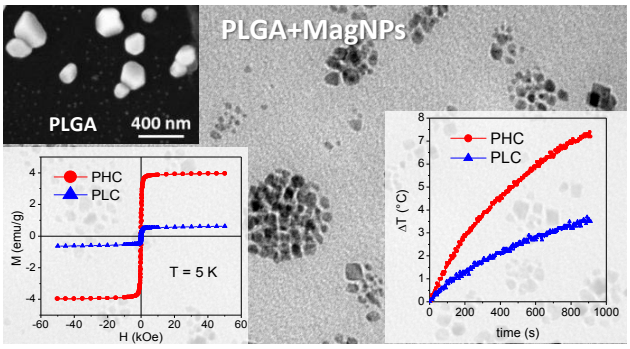
PLGA+MagNPs
PLGA
400 nm
PHC
PLC
T = 5 K
M (emu/g)
H (kOe)
PHC
PLC
ΔT (°C)
time (s)